ECS Journal of Solid State
Science and Technology

Electrical and Structural Properties of Two-Inch Diameter (001) α-Ga2O3 Films Doped with Sn and Grown by Halide Epitaxy

To cite this article before publication: Vladimir I Nikolaev *et al* 2022 *ECS J. Solid State Sci. Technol.* in press https://doi.org/10.1149/2162-8777/ac9edb

Electrical and Structural Properties of Two-Inch Diameter (001) α-Ga2O3 Films Doped with Sn and Grown by Halide Epitaxy

Journal:	*ECS Journal of Solid State Science and Technology*
Manuscript ID	JSS-102875
Manuscript Type:	Research Paper
Date Submitted by the Author:	03-Oct-2022

Complete List of Authors:	Nikolaev, Vladimir; National University of Science and Technology MISIS, Electronics Polyakov, Alexander; National University of Science and Technology MISIS, Electronics Stepanov, Sergey; NUST "MISiS", Semiconductor Electronics & the Physics of Semiconductors; Ioffe Institute, Laboratory of Shaped Crystals Physics; Perfect Crystals LLC Pechnikov, Alexey; NUST "MISiS", Semiconductor Electronics & the Physics of Semiconductors; Ioffe Institute, Laboratory of Shaped Crystals Physics; Perfect Crystals LLC Yakimov, Eugene; NUST "MISiS", Semiconductor Electronics & the Physics of Semiconductors; Russian Academy of Sciences, Institute of Microelectronics Technology and High Purity Materials Chernykh, Alexey; NUST "MISiS", Semiconductor Electronics & the Physics of Semiconductors Vasilev, Anton; NUST "MISiS", Semiconductor Electronics & the Physics of Semiconductors Shchemerov, Ivan; NUST "MISiS", Semiconductor Electronics & the Physics of Semiconductors Kochkova, Anastasia; National University of Science and Technology MISIS, Electronics Guzilova, Lyubov Guzilova; Perfect Crystals LLC Konovalev, Mikhail; National University of Science and Technology MISIS, Electronics Pearton, Stephen; University of Florida, Materials Science and Engineering

Keywords:	Deep level transient spectroscopy, Ga2O3, gallium oxide, Microelectronics - Semiconductor Materials, Semiconductors, Wide energy bandgap

Electrical and Structural Properties of Two-Inch Diameter (0001) α-Ga_2O_3 Films Doped with Sn and Grown by Halide Epitaxy

V.I. Nikolaev,[1,2] A.Y. Polyakov,[2] S. I. Stepanov,[1,2] A. I. Pechnikov,[1,2] E. B. Yakimov,[2,3] A.V. Chernykh,[2] A.A. Vasilev,[2] I.V. Shchemerov,[2] A.I. Kochkova,[2] L. Guzilova,[1,2] M. P. Konovalov,[2] and S. J. Pearton[4,*,z]

[1]Perfect Crystals LLC, Saint Petersburg 194223, Russia

[2.] National University of Science and Technology MISiS, Moscow 119049, Russia

[3]Institute of Microelectronics Technology RAS, Chernogolovka 142432, Russia

[4.] Department of Materials Science and Engineering, University of Florida, Gainesville, Florida 32611, USA

*Electrochemical Society Fellow.

[z]E-mail: spear@mse.ufl.edu

ABSTRACT

Two-inch diameter α-Ga_2O_3 films with thickness ~ 4 μm were grown on basal plane sapphire by Halide Vapor Phase Epitaxy (HVPE) and doped with Sn in the top ~1 μm from the surface. These films were characterized with High-Resolution X-ray Diffraction (HRXRD), Scanning Electron Microscope (SEM) imaging in the Secondary Electron (SE) and Micro-cathodoluminescence (MCL) modes, contactless sheet resistivity mapping, capacitance-voltage, current-voltage, admittance spectra, and Deep Level Transient Spectroscopy (DLTS) measurements. The edge and screw dislocations densities estimated from HRXRD data were respectively 7.4×10^9 cm^{-2} and 1.5×10^7 cm^{-2}, while the films had a smooth surface with a low density (~10^3 cm^{-2}) of circular openings with diameters between 10 and 100 μm. The sheet resistivity of the films varied over the entire 2-inch diameter from 200 to 500 Ω/square. The net donor concentration was ~10^{18} cm^{-3} near the surface and increased to ~4×10^{18} cm^{-3} deeper inside

the sample. The deep traps observed in admittance and DLTS spectra had levels at E_c-0.25 eV and E_c-0.35 eV, with concentration ~10^{15} cm^{-3} and E_c-1 eV with concentration ~10^{16} cm^{-3}.

I. INTRODUCTION

The metastable alpha-polymorph of the wide-bandgap Ga_2O_3 semiconductor has attracted growing scientific and practical interest recently owing to the high electric breakdown field exceeding that of the stable monoclinic β-Ga_2O_3 polymorph [1-8] and the possibility to grow α-Ga_2O_3 films and heterojunctions by Halide Vapor Phase Epitaxy (HVPE), mist Chemical Vapor Deposition (mist CVD) or Molecular Beam Epitaxy (MBE) with reasonable crystalline quality on mature α-Al_2O_3 (sapphire) substrates [1-4]. This emerging semiconductor is a potential next frontier material, especially for high-temperature and radiation hard applications. The advantages to using the α-Ga_2O_3 polymorph come from a higher bandgap than for β-Ga_2O_3 (5.2 eV versus 4.9 eV), higher symmetry (corundum versus monoclinic) and hence lower impact of anisotropy, the existence of a host of related oxides with transition and rare metals allowing fabrication of useful heterojunctions [9-28] and the possibility of solving, at least in principle, of the very acute problem of the lack of feasible p-type doping in all Ga_2O_3 polymorphs [29]. The device potential of α-Ga_2O_3 has been demonstrated by several groups [1-8, 30-33]. In addition, for displacement damage created by radiation, the displacement energy (E_D) for ultra-wide bandgap materials is given by the equation $E_D = 1.78\ (1/C_I)^3$, where C_I is the lattice constant in nm [30]. Since the displacement energy correlates with radiation hardness, the different polytypes of Ga_2O_3 exhibits superior radiation hardness [31].

In this paper we summarize the current state of research and recent progress in developing the electrical and structural quality of large diameter (2 inches) films of α-Ga_2O_3 grown by HVPE on basal plane sapphire substrates.

II.EXPERIMENTAL

Ga_2O_3 films were grown by HVPE on the sapphire substrates of c (0001) orientation as described previously [34-36]. The growth of the Ga_2O_3 films was performed at 500°C, with a fixed VI/III mole flow ratio of 4.2 and an average growth rate of 2.8 μm/h, on two-inch diameter, commercial basal plane sapphire substrates. The overall thickness of the films was ~4 μm. The samples were heavily doped with Sn down to a depth of ~ 1 μm from the surface, while the lower part of the films was nominally undoped. Sn was provided by addition of Sn salt vapor to the Ar gas transport flow. Compared to the previous design [34-36], the diameter of the growth chamber was increased in order to be able to accommodate larger substrates with diameter up to 3 inches. The hydrodynamics of the reactor was optimized to improve the uniformity of the film thickness and doping.

The phase composition was determined from Θ-2Θ x-ray diffraction scans, while the crystalline quality was assessed by measurement of the Full Width at Half-Maximum (FWHM) of high-resolution, triple-axis symmetric and asymmetric rocking curves. The x-ray reflections used were (0006) and (10-18). The details can be found in our earlier papers [37-39].

For electrical measurements, Au/Ti Ohmic contacts in the form of stripes and circular semi-transparent Ni contacts with diameter 1 mm were deposited on the film surface using e-beam evaporation through a shadow mask. The thickness of the Au/Ti pads was 80nm/20 nm, and after deposition they were annealed at 300ºC for 2 minutes in flowing nitrogen. The thickness of Ni contacts was 20 nm [37-39].

The morphology of the films was characterized by Scanning Electron Microscope (SEM) mapping in the Secondary Electrons (SE) and Microcathodoluminescence (MCL) imaging modes. Also at each point of interest the MCL spectra were measured at room temperature (the setups are described in detail in Ref. [37-39]).

The electrical uniformity of the films was assessed by contactless resistivity measurements using the UHF measurements system allowing measurements of sheet resistivity in the range from 100 to 3000 Ω/square. This is based on measurements of the ratio of intensities of the incident and reflected power of UHF wave falling normally at the studied sample at 10 GHz in the wave-guiding system. The system was calibrated by measurements of the sheet resistivity of AlGaN/GaN heterojunctions with known sheet resistivities from independent van der Pauw measurements. The probe diameter was 14 mm, the distance between the measured points was 7 mm. In principle, the system allows to measure the mobility by monitoring the magnetoresistance, but the signal was not reliable because the mobility of the electrons was below the sensitivity limit of 100 $cm^2/V\times s$.

The samples were characterized by capacitance versus frequency C-f, capacitance versus voltage (C-V) profiling, admittance spectra (AS) , Deep Level Transient Spectroscopy (DLTS) [40], current-voltage IV measurements. These experiments were carried out in the temperature range 77-500K. The temperature was either stabilized at the desired value with the accuracy better than 0.1K or kept at the sweeping rate easily regulated between 0.1K/min and 3K/min, generally the sweeping range used was close to 1-2 K/min. Detailed descriptions of experimental setup can be found in our earlier papers [41-35].

III.RESULTS and DISCUSSION

XRD measurements of the half of the two-inch grown film showed that it is single-phase α-Ga_2O_3, with the FWHM of the symmetric (0006) reflection varying between 13 arcminutes and 15 arcminutes, and the FWHM of the asymmetric (10-18) asymmetric reflection between 14 and 17 arc. minutes. Measurements of the film thickness on the cross section of the film gave the thickness of 4 µm. The surface of the film was quite smooth, but occasionally showed the presence of round depressions with a small hillock inside and the diameter varying from ~10 µm to ~50 µm . The density of such defects varied along the diameter from 0 to about 10^3 cm^{-2}. In panchromatic MCL images the edge of the defect displayed a higher intensity, whereas the inner part looked dark (Fig. 1 displays one such defect imaged in secondary electrons mode (upper image) and panchromatic MCL (lower image)). MCL spectra measured at two different points of the film are shown as black lines in Fig.2. They could be reliably deconvoluted into five Gaussian MCL bands peaked at 2.55, 2.82, 2.67, 2.4, and 3.7 eV photon energies (the overall spectra obtained from the fitting procedure are shown in red and can be compared to experimentally observed spectra shown in black lines). The distribution of the MCL intensity of different bands along the diameter starting with the sample facet and taken from the area of

425×320 μm^2 with a step of 1.1 mm is shown in Fig. 3. It can be seen that the 3.7 eV UV band intensity is the lowest towards the center of the wafer (U-like distribution) and is in antiphase with the intensities of the visible MCL bands.

Fig. 4 displays the schematic of the samples with the positions of the points of contactless control of the sheet resistivity R_{sh} (the diameter of the probe in contactless Rsh measurements was 14 mm, the vertical distance between the control points was 6.25 mm, the distance between the two rows of control points was 7 mm, the distance to the edge of the wafer for the right-hand-side row of points was 7 mm. In each control point three consecutive measurements were made and the average of these measurements was assigned to the local R_{sh}. The data are presented in Table I. Fig. 5 gives the pictorial distribution of the measured values. It can be seen that the spread of the sheet resistivities is still considerable and the doping uniformity requires further optimization.

More detailed electrical measurements were performed using the Schottky diodes characterization. Fig. 6 displays the current-voltage characteristic of one of the studied Schottky diodes on the sample cut from the middle part of the wafer. The leakage is relatively high (the reverse current density at -1V close to 10^{-3} A/cm^2), the series resistance deduced from the IV plot was considerable, close to 220 Ω, the ideality factor reasonably close to unity ($n_{ideality}$=1.3), with the saturation current density deduced from the forward IV characteristic estimated as 1.4×10^{-6} A/cm^2.

The 1/C^2 versus voltage plot obtained at room temperature at 10 kHz is shown in Fig. 7(a). The doping is obviously dependent on depth as is clear from the concentration versus depth profile calculated from C-V data in Fig. 7(b). The net donor concentration is close to 10^{18} cm^{-3} near the surface and increases when one moves deeper inside the sample.

Some idea of the types of centers determining the carrier concentration can be deduced from admittance spectra measured on this Schottky diode. Fig. 8(a) displays the temperature dependence of capacitance measured at -0.2V at various frequencies , Fig. 8(b) shows the temperature dependencies of AC conductance G normalized by the angular frequency □=2□f for various measurement frequencies f [40]. As the temperature decreases the Fermy level consecutively crosses the states with levels at E_c-0.25 eV (electron capture cross section σ_n= 2.7×10^{-14} cm^2), E_c-0.35 eV (σ_n=8.4×10^{-17} cm^2), and E_c-0.5 eV (σ_n=9.4×10^{-16} cm^2).

Detailed deep level spectra of the sample were measured by DLTS. The measured spectrum is shown in Fig. 9. It was obtained with reverse bias kept at -1V, the forward pulse of 0V (the length of 50 ms). The centers detected were the electron traps with the level E_c-0.25 eV (σ_n =1.3×10^{-16} cm^2), E_c-0.55 eV (σ_n =10×16 cm2), E_c-1 eV (σ_n =10^{-14} cm^2). The estimated concentrations of the centers were respectively, 1.7×10^{15} cm^{-3}, 1.3×10^{15} cm^{-3} and 1.5×10^{16} cm^{-3}.

CONCLUSIONS

Our measurements show that moderately n-type doped 2-inch-diameter films can be grown by the HVPE technique with the net donor doping at the surface of~ 10^{18} cm^{-3}, but increasing to higher concentration close to 4×10^{18} cm^{-3} deeper inside. The spatial distribution of doping density measured across the sample sill displays a considerable spread. Both the spatial variations of doping across the area and the depth variations of doping are the result of our adopted doping method by using evaporation of the volatile Sn salt and a considerable contribution to the density of electrically active centers of native-defects-related states. We are currently experimenting with switching to Si doping from SiH_4 instead of Sn doping [1], but have not succeeded yet in achieving controlled doping that way.

The crystalline perfection of the 4-µm-thick films is close to the one commonly reported. If one judges by the FWHM values f the symmetrical and asymmetrical HRXRD reflections the dislocation densities of the edge dislocations and screw dislocations in the studied samples are 7.4×10^{9} cm^{-2} and 1.5×10^{7} cm^{-2} respectively. The origin of the circular defects in the film has to be studied in more detail, but fortunately their density is quite moderate, although if they appear in the active region of the device they would certainly lead to device failures.

The types of defects observed in DLTS and admittance spectra are common to the α-Ga_2O_3 films deposited by HVPE on sapphire [2, 4]. The nature of these defects requires further study, but are known to influence the interfacial characteristics and performance devices [46,47].

ACKNOWLEDGMENTS

The work at NUST MISiS and by co-authors at Perfect Crystals and IMT RAS at IMT RAS was supported in part by the Russian Science Foundation, grant no. 19-19-00409. The work at UF was performed as part of Interaction of Ionizing Radiation with Matter University Research Alliance (IIRM-URA*)*, sponsored by the Department of the Defense, Defense Threat Reduction Agency under award HDTRA1-20-2-0002. The content of the information does not necessarily reflect the position or the policy of the federal government, and no official endorsement should be inferred. The work at UF was also supported by NSF DMR 1856662 (James Edgar).

There are no competing financial interests in this paper. All data that support the findings of this study are included within the article.

REFERENCES

1. Gallium Oxide: Materials Properties, Crystal Growth, and Devices, ed. Masataka Higashiwaki and Shizuo Fujita (Springer Series in Materials Science ISBN 978-3-030-37152-4 ISBN 978-3-030-37153-1, 2020) parts 1-4
2. Mahitosh Biswas and Hiroyuki Nishinaka, APL Mater. 10, 060701 (2022).
3. Elaheh Ahmadi and Yuichi Oshima, J. Appl. Phys. 126, 160901 (2019).
4. Takuya Maeda, Mitsuru Okigawa, Yuji Kato, Isao Takahashi, and Takashi Shinohe, AIP Adv. 10, 125119 (2020).
5. A. Hassa, P. Storm, M. Kneiß, D. Splith, H. von Wenckstern, M. Lorenz and M. Grundmann, Phys. Status Solidi B, 258, 2000394 (2021).
6. H. Zhang, L. Yuan, X. Tang, J. Hu, J. Sun, Y. Zhang, Y. Zhang, and R. Jia, IEEE T. Power Electr. 35, 5157 (2020).
7. A. Y. Polyakov, V. I. Nikolaev, E. B. Yakimov, F. Ren, S. J. Pearton, and J. Kim, J. Vac. Sci. Technol. A 40, 020804 (2022).
8. Zhengpeng Wang, Xuanhu Chen, Fang-Fang Ren, Shulin Gu and Jiandong Ye, J. Phys D: Appl. Phys, 54, 043002 (2021).
9. C. Cora, Z. Fogarassy, R. Fornari, M. Bosi, A. Rečnik, and B. Pecz, Acta Mater.183, 216 (2020).
10. A. F. M. A. U. Bhuiyan, Z. Feng, J. M. Johnson, H.-L. Huang, J. Sarker, M. Zhu, M. R. Karim, B. Mazumder, J. Hwang, and H. Zhao, APL Mater. 8, 031104 (2020).
11. M. Hilfiker, U. Kilic, M. Stokey, R. Jinno, Y. Cho, H. G. Xing, D. Jena, R. Korlacki, and M. Schubert, Appl. Phys. Lett. 119, 092103 (2021).
12. K. Uno, R. Jinno, and S. Fujita, J. Appl. Phys. 131, 090902 (2022).
13. J. A. Spencer, A. L. Mock, A. G. Jacobs, M. Schubert, Y. Zhang, and M. J. Tadjer, Appl. Phys. Rev. 9, 011315 (2022).

14. D. Yang, B. Kim, T. H. Eom, Y. Park, and H. W. Jang, Electron. Mater. Lett.18, 113 (2022).

15. R. Schewski, G. Wagner, M. Baldini, D. Gogova, Z. Galazka, T. Schulz, T. Remmele, T. Markurt, H. von Wenckstern, M. Grundmann, O. Bierwagen, P. Vogt, and M. Albrecht, Appl. Phys. Express 8, 011101 (2015).

16. M. Kracht, A. Karg, M. Feneberg, J. Bläsing, J. Schörmann, R. Goldhahn, and M. Eickhoff, Phys. Rev. Appl. 10, 024047 (2018).

17. Y. Oshima, K. Kawara, T. Shinohe, T. Hitora, M. Kasu, and S. Fujita, APL Mater. 7, 022503 (2019).

18. K. Kawara, Y. Oshima, M. Okigawa, and T. Shinohe, Appl. Phys. Express 13, 075507 (2020).

19. Andrew Venzie, Amanda Portoff, W. Beall Fowler, Michael Stavola, Dae Woo Jeon, Jihyun Kim and S. J. Pearton, Appl. Phys. Lett. 120, 192101 (2022).

20. Alexander Y. Polyakov, Vladimir I. Nikolaev, Igor N. Meshkov, Krzysztof Siemek, Petr B. Lagov, Eugene B. Yakimov, Alexei I. Pechnikov, Oleg S. Orlov, Alexey A. Sidorin, Sergey I. Stepanov, Ivan V. Shchemerov, Anton A. Vasilev, Alexey V. Chernykh, Anton A. Losev, Alexandr D. Miliachenko, Igor A. Khrisanov, Yu.S. Pavlov, U.A. Kobets and S. J. Pearton, J. Appl. Phys. 132, 035701 (2022).

21. A. Sharma and U. Singisetti, Appl. Phys. Lett. 118, 032101 (2021).

22. A. Segura, L. Artus, R. Cusco, R. Goldhahn, and M. Feneberg, Phys. Rev. Mater. 1, 024604 (2017).

23. M. Hilfiker, R. Korlacki, R. Jinno, Y. Cho, H. G. Xing, D. Jena, U. Kilic, M. Stokey, and M. Schubert, Appl. Phys. Lett. 118, 062103 (2021).

24. M. Feneberg, J. Nixdorf, M. D. Neumann, N. Esser, L. Artus, R. Cusco, T. Yamaguchi, and R. Goldhahn, Phys. Rev. Mater. 2, 044601 (2018).

25. M. Stokey, R. Korlacki, M. Hilfiker, S. Knight, S. Richter, V. Darakchieva,R. Jinno, Y. Cho, G. H. Xing, D. Jena, Y. Oshima, K. Khan, E. Ahmadi, and M. Schubert, Phys. Rev. Mater. 6, 014601 (2022).

26. S. I. Kan, S. Takemoto, K. Kaneko, I. Takahashi, M. Sugimoto, and T. Shinohe, Appl. Phys. Lett. 113, 212104 (2018).

27. J. G. Hao, H. H. Gong, X. H. Chen, Y. Xu, F. F. Ren, and S. L. Gu, Appl. Phys. Lett. 118, 261601 (2021).

28. Kentaro Kaneko, Shizuo Fujita, and Toshimi Hitora, J. Appl. Phys. 57, 02CB18 (2018).

29. Alexandros Kyrtsos, Masahiko Matsubara, and Enrico Bellotti, Appl. Phys. Lett. 112, 032108 (2018).

30. M. Shur, ECS Transactions, 109 (8) 21 (2022).

31. Xinyi Xia, Jian Sian Li, Ribhu Sharma, Fan Ren, Md Abu Jafar Rasel, Sergei Stepanoff, Nahid Al Mamun, Aman Haque, Douglas E. Wolfe, Sushrut Modak, Leonid Chernyak, Mark E. Law, Ani Khachatrian and S. J. Pearton, ECS J. Sol.State. Sci.Technol. 11, 095001 (2022).

32. H. Peelaers, J.L. Varley and C.G. Van de Walle, APL Mater. 7, 022519 (2019).

33. Kentaro Kaneko, Yasuhisa Masuda, Shin-ichi Kan, Isao Takahashi, Yuji Kato, Takashi Shinohe, and Shizuo Fujita, Appl. Phys. Lett. 118, 102104 (2021).

34. A. Y. Polyakov, N. B. Smirnov, I. V. Shchemerov, E. B. Yakimov , V. I. Nikolaev, S. I. Stepanov, A. I. Pechnikov, A. V. Chernykh , K. D. Shcherbachev, A. S. Shikoh, A. Kochkova, A. A. Vasilev, and S. J. Pearton, APL Mater. 7, 051103 (2019).

35. A. Y. Polyakov, V. I. Nikolaev, S. I. Stepanov, A. I. Pechnikov, E. B. Yakimov, N. B. Smirnov, I. V. Shchemerov, A. A. Vasilev, A. I. Kochkova, A.V. Chernykh, and S. J. Pearton, ECS J. Solid State Sci. Technol., 9, 045003 (2020).

36. Alexander Polyakov, Vladimir Nikolaev, Sergey Stepanov, Alexei Almaev, Alexei Pechnikov, Eugene Yakimov, Bogdan O. Kushnarev, Ivan Shchemerov, Mikhail

Scheglov, Alexey Chernykh, Anton Vasilev, Anastasia Kochkova, and Stephen J. Pearton, J. Appl. Phys. 131, 215701 (2022).

37. E. B. Yakimov and A. Y. Polyakov, "Defects and carrier lifetimes in Ga_2O_3," in Wide Bandgap Semiconductor-Based Electronics, edited by Fan Ren and S. Pearton (IOP Publishers, 2020), Chap. 5
38. E. B. Yakimov, A. Y. Polyakov, I. V. Shchemerov, N. B. Smirnov, A. A. Vasilev, P. S. Vergeles, E. E. Yakimov, A. V. Chernykh, A. S. Shikoh, F. Ren, and S. J. Pearton. APL Mater. 8, 111105 (2020).
39. A. Y. Polyakov, N. B. Smirnov, I. V. Schemerov, A. V. Chernykh, E. B. Yakimov, A. I. Kochkova, A. N. Tereshchenko, and S. J. Pearton, ECS J. Solid State Sci. Technol, 8 (7) Q3091(2019).
40. Capacitance spectroscopy of semiconductors, ed. Jian V. Li and Giorgio Ferrari (Pan Stanford Publishing Pte Ltd, Singapore, 2018) 437 pp
41. A.Y. Polyakov, N. B. Smirnov, I.V. Shchemerov, S.J. Pearton, F. Ren, A.V. Chernykh, P.B. Lagov and T.V. Kulevoy, APL Materials 6, 096102 (2018).
42. A. Y. Polyakov, N. B. Smirnov, I V Shchemerov, A A Vasilev, E B Yakimov, A V Chernykh, A I Kochkova, P. B. Lagov, Yu S Pavlov, O F Kukharchuk, A A Suvorov, N S Garanin, In-Hwan Lee, Minghan Xian, Fan Ren and S. J. Pearton, J. Phys. D: Appl. Phys. 53, 274001(2020).
43. A. Y. Polyakov, In-Hwan Lee, N B Smirnov, I V Shchemerov, A A Vasilev, A V Chernykh and S J Pearton, J. Phys. D: Appl. Phys. 53, 304001(2020).
44. A. Y. Polyakov, N. B. Smirnov, I. V. Shchemerov, S. J. Pearton, F. Ren, A. V. Chernykh, P. B. Lagov, and T. V. Kulevoy, APL Mater. 6, 096102 (2018).
45. Alexander Y. Polyakov, Nikolai B. Smirnov, In-Hwan Lee and Stephen J. Pearton, J. Vac. Sci. Technol B 33, 061203 (2015).

46. Yuan Yuan, Weibing Hao, Wenxiang Mu, Zhengpeng Wang, Xuanhu Chen, Qi Liu, Guangwei Xu, Chenlu Wang, Hong Zhou, Yanni Zou, Xiaolong Zhao, Zhitai Jia, Jiandong Ye, Jincheng Zhang, Shibing Long, Xutang Tao, Rong Zhang, Yue Hao, Fundamental Research 1, 697 (2021).

47. Chowdam Venkata Prasad and You Seung Rim, Materials Today Physics 27, 100777 (2022).

Table I. The results of contactless R_{sh} mapping

Point #	R_{sh} (□/square)			
	Measurement 1	Measurement 2	Measurement 3	Average
1	294	300	289	294
2	254	254	241	250
3	216	217	212	215
4	207	196	212	205
5	418	406	350	391
6	736	728	654	706
7	349	317	378	348
8	368	412	370	383
9	322	345	320	329
10	293	305	278	292
11	500	534	496	510
12	558	410	449	472

FIGURE CAPTIONS

Fig. 1. Images of defects in secondary electrons (upper) and panchromatic MCL SEM modes

Fig. 2 (Color online) MCL spectra measured at two different points with the probing beam current of 1 nA and accelerating voltage of 10 kV; experimental spectra are presented by the black line, the red line is the result of fitting the spectrum by 5 Gaussian bands peaked at 2.55 eV (blue line), 2.82 eV (magenta line), 2.67 eV (violet line), 2.4 eV (olive line) 3.7 eV (wine line), (a) was taken near the lower edge, (b) taken near the center of the wafer

Fig. 3 (Color online) The spatial distributions of the intensity of the MCL bands along the wafer diameter obtained by fitting the experimental local MCL spectra

Fig. 4. (Color online) Schematic representation of the sheet resistivity contactless measurements points distribution and characteristic dimensions involved

Fig. 5 (Color online) The chart of the sheet resistivity distribution

Fig. 6 (Color online) Room temperature IV characteristic of the measured diode

Fig. 7 (Color online) (a) Room temperature $1/C^2$ versus V plot; (b) charge concentration profile calculated from the $1/C^2$ versus V plot

Fig. 8 (Color online) The temperature dependence of AC conductance G normalized by the angular frequency □=2□f for several frequency measurements: 20 Hz (red line), 100 Hz (blue line), 300 Hz (magenta line), 500 Hz (olive line)

Fig. 9 (Color online) DLTS spectrum taken with reverse bias -1V, forward bias pulse 1V (50 ms), time windows 200 ms/2000 ms, measured at the probing frequency of 10 kHz

FIGURES

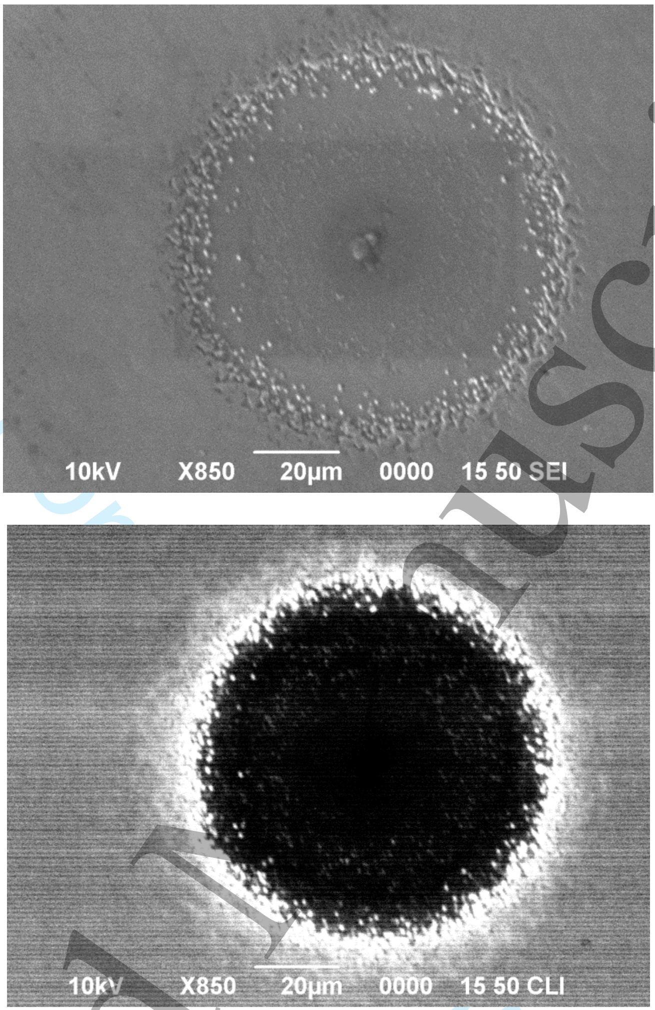

Fig. 1. Images of defects in secondary electrons (upper) and panchromatic MCL SEM modes

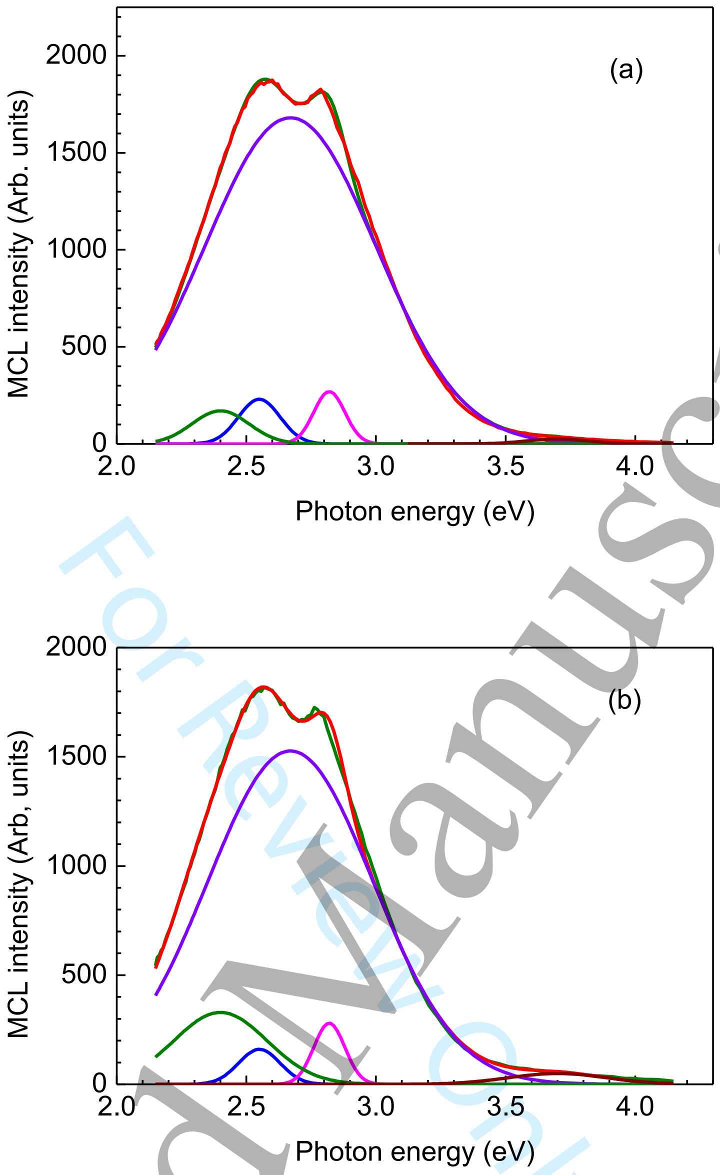

Fig. 2 (Color online) MCL spectra measured at two different points with the probing beam current of 1 nA and accelerating voltage of 10 kV; experimental spectra are presented by the black line, the red line is the result of fitting the spectrum by 5 Gaussian bands peaked at 2.55 eV (blue line), 2.82 eV (magenta line), 2.67 eV (violet line), 2.4 eV (olive line) 3.7 eV (wine line), (a) was taken near the lower edge, (b) taken near the center of the wafer

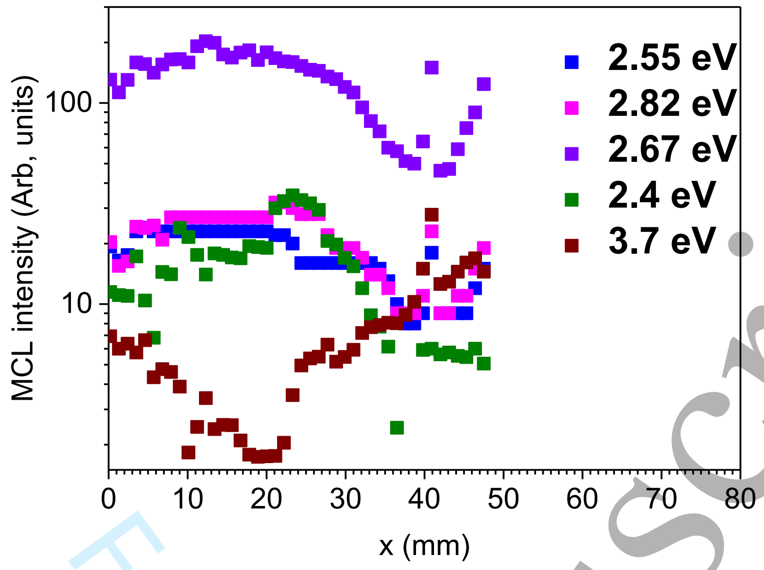

Fig. 3 (Color online) The spatial distributions of the intensity of the MCL bands along the wafer diameter obtained by fitting the experimental local MCL spectra

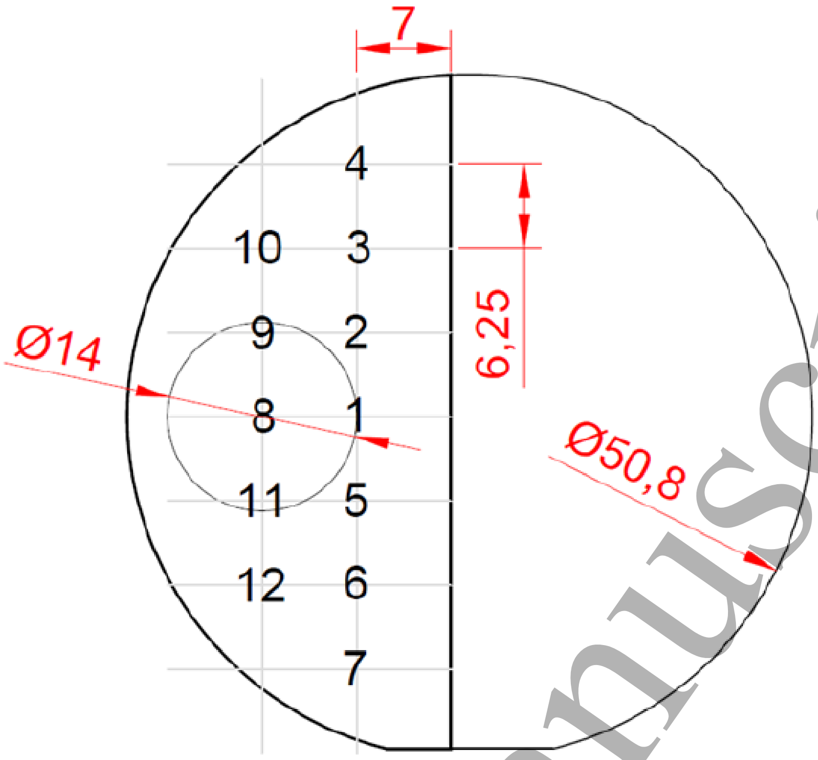

Fig. 4(Color online) Schematic representation of the sheet resistivity contactless measurements points distribution and characteristic dimensions involved

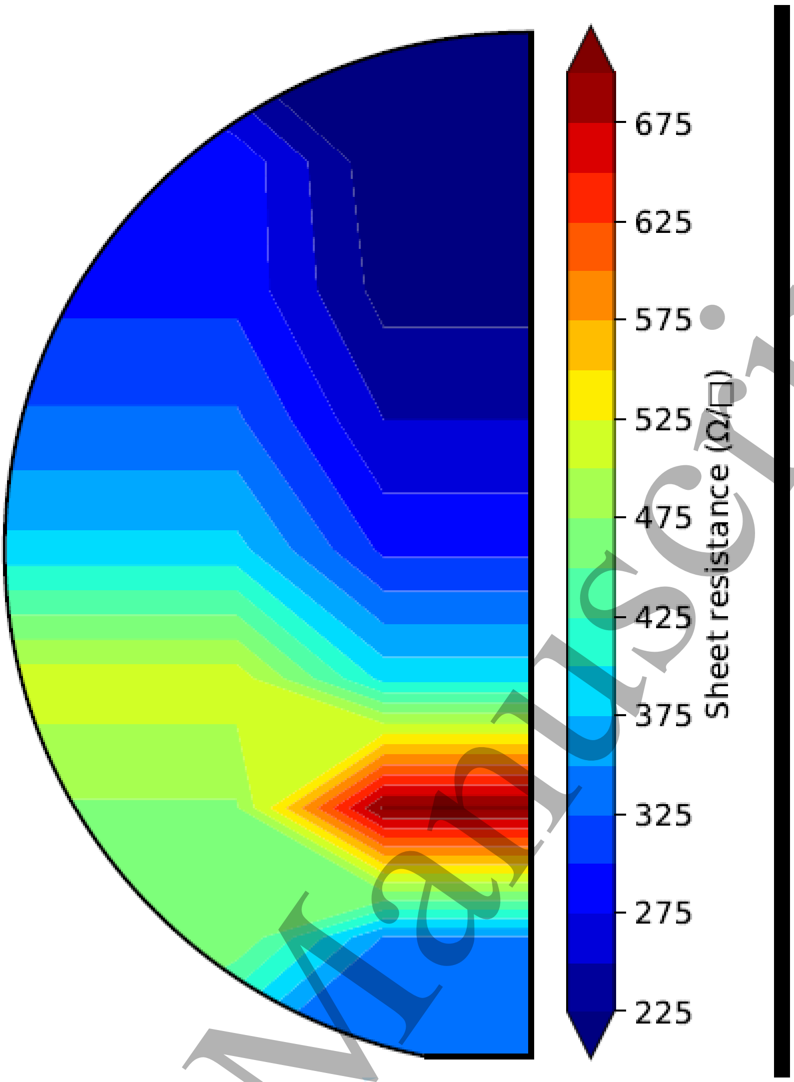

Fig. 5 (Color online) The chart of the sheet resistivity distribution

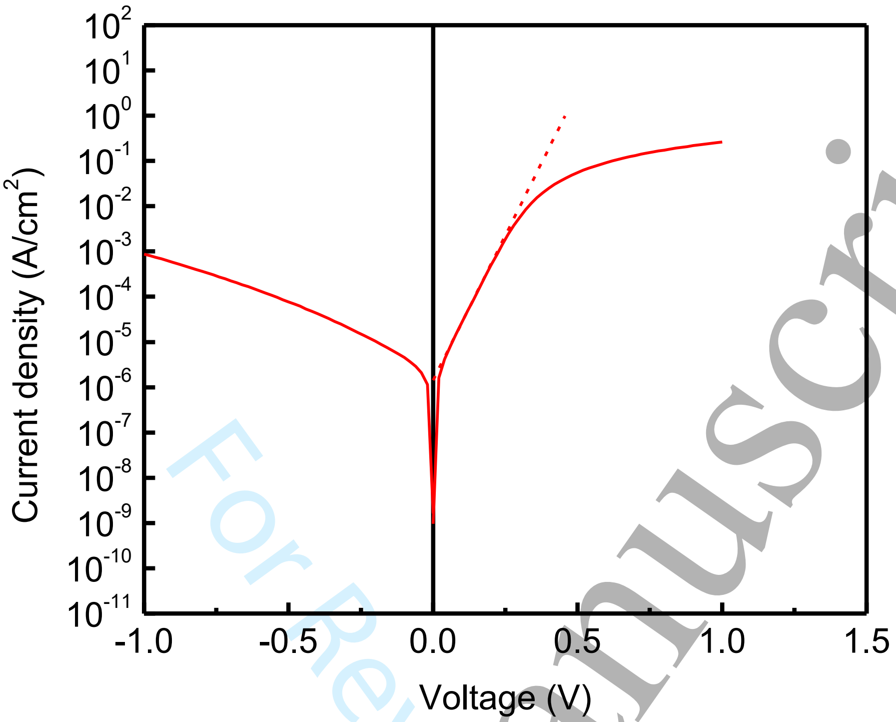

Fig. 6 (Color online) Room temperature IV characteristic of the measured diode

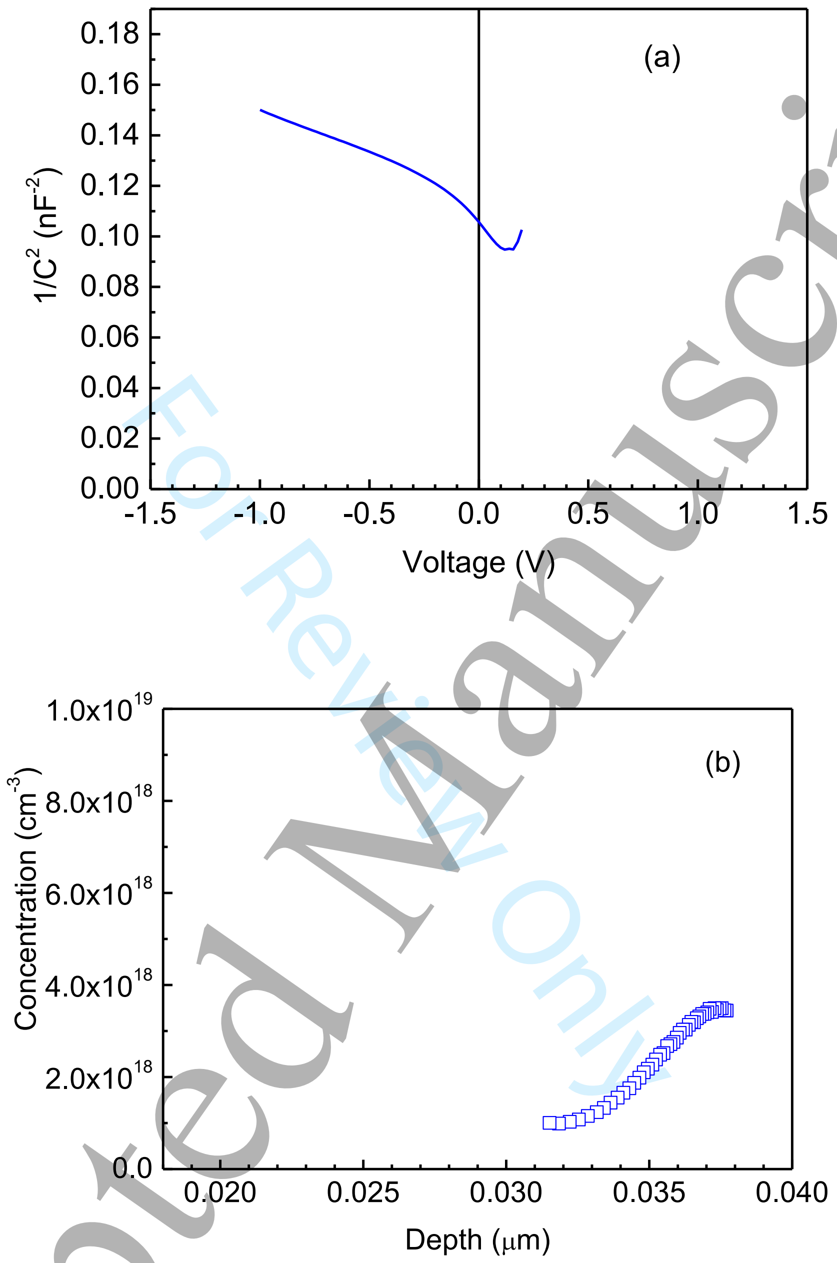

Fig. 7 (Color online) (a) Room temperature $1/C^2$ versus V plot; (b) charge concentration profile calculated from the $1/C^2$ versus V plot

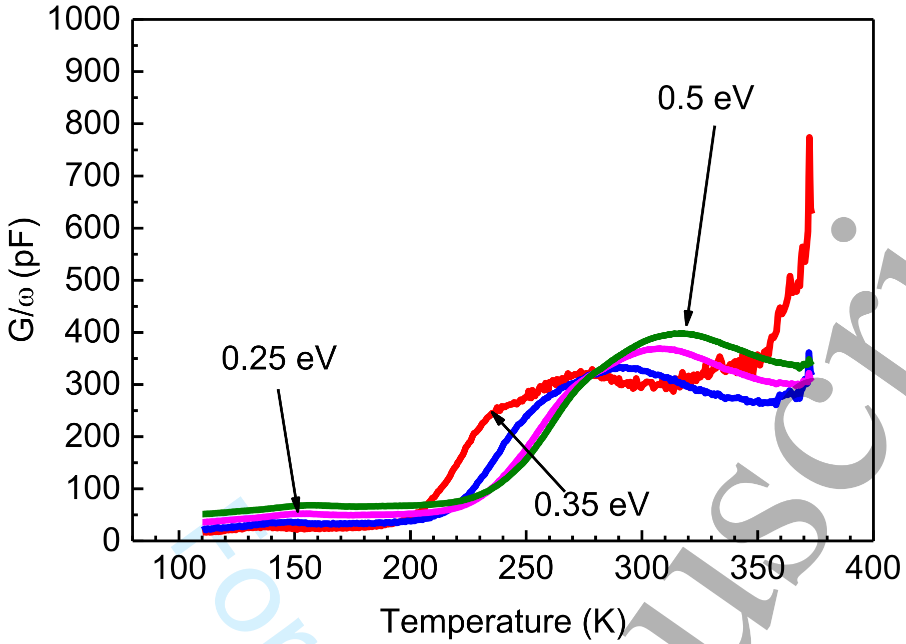

Fig. 8 (Color online) The temperature dependence of AC conductance G normalized by the angular frequency $\omega=2\pi f$ for several frequency measurements: 20 Hz (red line), 100 Hz (blue line), 300 Hz (magenta line), 500 Hz (olive line)

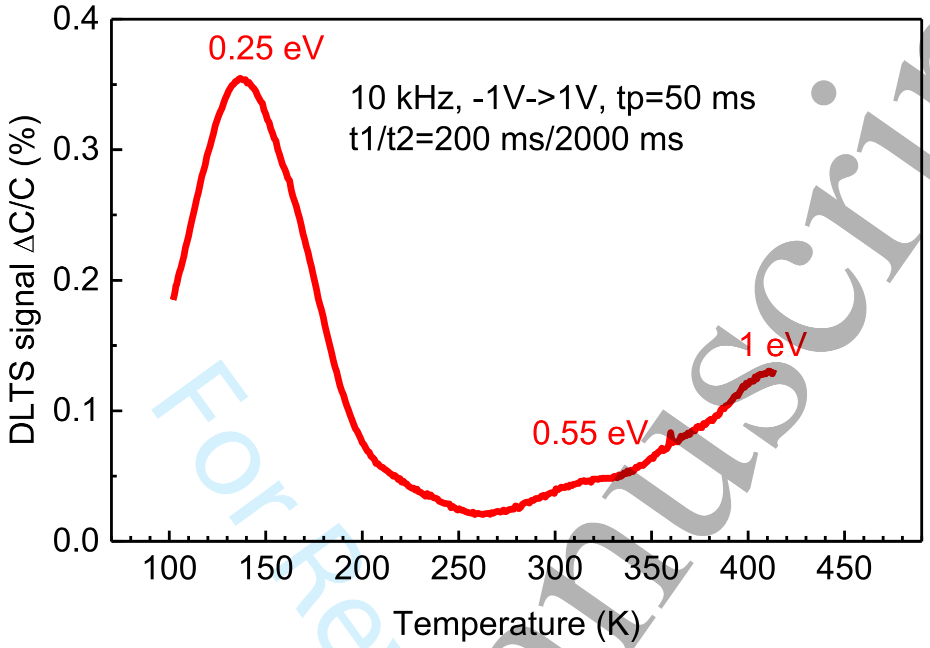

Fig. 9 (Color online) DLTS spectrum taken with reverse bias -1V, forward bias pulse 1V (50 ms), time windows 200 ms/2000 ms, measured at the probing frequency of 10 kHz